

# Nonadiabatic Effects on Proton Transfer Rate Constants in a Nanoconfined Solvent

Being J. Ka and Ward H. Thompson\*

Department of Chemistry, University of Kansas, Lawrence, Kansas 66045

Received: December 11, 2009; Revised Manuscript Received: April 16, 2010

Nonadiabatic effects on the reaction rate constant of a model phenol–amine proton transfer system in a nanoconfined solvent have been investigated by employing classical mapping in conjunction with a reactive flux approach. It is observed that allowing nonadiabatic transitions makes the transition state more accessible thermodynamically but decreases the reactive flux due to increased transition state recrossing, resulting in an overall reduction in the rate constant by more than a factor of 2. The physical origins of these features are discussed.

## 1. Introduction

Proton transfer reactions are ubiquitous in chemistry, biology, and physics. At the same time, they present particular challenges in their theoretical description, not least of which is the importance of quantum mechanical effects associated with the proton's small mass. This leads to significant, and sometimes dramatic, tunneling contributions to proton transfer rate constants. To accurately describe these, more than one proton vibrational quantum state must be accounted for along with transitions between these states. Here, we consider these nonadiabatic contributions to the proton transfer reaction rate constants for a model reaction complex in a nanoconfined solvent.

Reactions in nanoconfined solvents can differ dramatically from those in bulk solvents due to changes in both equilibrium and dynamical properties. Among these are molecular-level structuring of the liquid, free energies that depend on position, slower diffusional and reorientational time scales, and altered reaction mechanisms. The nature and magnitude of the effects one finds upon nanoconfinement depends on the observable of interest as well as the properties of the confining framework, for example, size, shape, rigidity, and chemical functionality. While some experimental<sup>1–7</sup> and theoretical<sup>8–10</sup> studies on charge transfer in nanoconfined solvents have been reported in the literature, a full understanding of how the mechanisms and rate constants of charge transfer reactions are affected by nanoscale confinement is still lacking. Filling this gap will assist in the development of design principles for applications of mesoporous materials in catalysis, sensing, and separations.

Here, we address this issue in the context of a model phenol–amine intramolecular proton transfer reaction occurring in methyl chloride solvent confined within a spherical, hydrophobic cavity of radius 1 nm. This system has already been investigated through calculation of reaction free energy curves<sup>8</sup> and vibrationally adiabatic mixed quantum-classical molecular dynamics<sup>9</sup> in which the proton is described quantum mechanically and the rest of the system classically. These studies identified significant changes in the reaction free energy surfaces and mechanism upon confinement in a nanoscale cavity. Specifically, Li and Thompson<sup>8</sup> showed that the proton transfer changes from endoergic to exoergic as the radial position

of the reaction complex is shifted from near the cavity wall to the center of the cavity. It was also found that the proton transfer mechanism in the nanoconfined solvent involves not only the collective solvent coordinate, which is the reaction coordinate for a bulk proton transfer reaction, but also the reaction complex position in the cavity. Subsequent vibrationally adiabatic simulations<sup>9</sup> showed that both the reaction exoergonicity and the vibrationally adiabatic rate constant increase as the cavity size increases. In this work, we address the role of tunneling by including vibrationally nonadiabatic dynamics in the proton quantum states.

While there are a number of approaches<sup>11–23</sup> for incorporating nonadiabatic dynamics, we use a reactive flux approach<sup>24,25</sup> combined with a classical mapping description.<sup>26–29</sup> In the reactive flux approach,<sup>24,25</sup> the calculation of the reaction rate constant is divided into two components: the probability of finding the reactants reaching the transition state and the rate of formation of products starting from the transition state. In this way, it permits the computation of rate constants for reactions with large activation energies for which the time scale for barrier crossing can be long. Moreover, it provides insight into the contributions to the rate constant, for example, equilibrium or dynamical, based on this decomposition. However, implementing the reactive flux approach while including nonadiabatic transitions can be challenging. The classical mapping approach<sup>26–29</sup> used here is a mean field method in which the classical degrees-of-freedom respond to a quantum mechanical state that is a superposition which in turn evolves according to the classical trajectory. It is important to note that the classical mapping approach involves dynamics on a state-averaged potential energy surface, which is a better approximation in regions of strong nonadiabatic coupling.<sup>14,18</sup> For a proton transfer reaction, this corresponds to the transition state region where reactivity is determined and where the trajectories are initiated in the reactive flux approach. Thus, the classical mapping approximation should be useful in this context, since the mean field description may accurately describe the strong coupling region dynamics in the vicinity of the transition state.

In implementing these calculations, we investigate not only the effect of vibrational nonadiabaticity on the reaction rate constant, but also a common assumption about the vibrational state populations at the transition state: Is it reasonable to assume that reactive flux trajectories initiated at the transition state should always begin in the ground vibrational state? This

\* To whom correspondence should be addressed. E-mail: wthompson@ku.edu.

assumption has been used in previous studies of nonadiabatic reaction rate constants for proton transfer.<sup>11,16</sup> Although the trajectories can undergo nonadiabatic transitions as they evolve, the excited vibrational state population at the transition state is implicitly taken to be zero.

The remainder of the paper is organized as follows. The theoretical approaches used to calculate vibrationally adiabatic and vibrationally nonadiabatic reaction rate constants are outlined in section 2. The model phenol–amine proton transfer complex, the nanoconfined solvent system, and the simulation details are described in section 3. The computational results are presented and discussed in section 4, and some concluding remarks are offered in section 5.

## 2. Methods

In this section, we outline the approaches for vibrationally adiabatic and nonadiabatic mixed quantum-classical (MQC) molecular dynamics (MD) including the calculation of reaction rate constants.

**2.1. Vibrationally Adiabatic Dynamics. 2.1.1. Adiabatic MQC-MD Approach.** Here, we consider the case of a single quantum mechanical degree-of-freedom interacting with a classical bath. In the context of the proton transfer system examined in this work, the former is the proton position within a reaction complex (the O–H distance in the linear phenol–amine hydrogen bond) and the latter are the remaining degrees-of-freedom of the reaction complex as well as the solvent molecules. If the quantum mechanical degree-of-freedom is denoted as  $r$  with corresponding momentum  $p_r$ , the Hamiltonian for the classical degrees-of-freedom can be written as<sup>32</sup>

$$H_n(\mathbf{P}, \mathbf{Q}, \mathbf{p}_e, \mathbf{e}) = \sum_i \frac{\mathbf{p}_i^2}{2m_i} + \sum_i \frac{\mathbf{p}_{e,i}^2}{2I_i} + E_n(\mathbf{Q}, \mathbf{e}) + \sum_i \lambda_i (\mathbf{e}_i \cdot \mathbf{e}_i - 1) \quad (1)$$

Here,  $(\mathbf{Q}, \mathbf{P})$  are the center-of-mass coordinates and momenta of the reaction complex and solvent molecules,  $(\mathbf{e}, \mathbf{p}_e)$  are the orientational unit vectors and conjugate momenta of these molecules (assuming they are rigid),  $\lambda_i$  is a Lagrange undetermined multiplier ensuring the normalization of the orientational vectors, and  $E_n(\mathbf{Q}, \mathbf{e})$  is the (proton)  $n$ th vibrationally adiabatic energy for fixed classical coordinates  $\mathbf{Q}$  and  $\mathbf{e}$ . This last is obtained by the solution of the vibrationally adiabatic Schrödinger equation in  $r$ :

$$\hat{h}_r(\hat{r}; \mathbf{Q}, \mathbf{e}) \psi_n(r; \mathbf{Q}, \mathbf{e}) = E_n(\mathbf{Q}, \mathbf{e}) \psi_n(r; \mathbf{Q}, \mathbf{e}) \quad (2)$$

where

$$\hat{h}_r(\hat{r}; \mathbf{Q}, \mathbf{e}) = \frac{\hat{p}_r^2}{2m_H} + V_{gr}(\hat{r}; \mathbf{Q}, \mathbf{e}) \quad (3)$$

and  $V_{gr}$  is the electronic ground state potential energy. The equations of motion and integration algorithm appropriate for eq 1 have been described in detail in ref 32.

In addition to propagating the dynamics according to this vibrationally adiabatic MQC Hamiltonian, eq 1, it is sometimes necessary to propagate trajectories under the influence of a biasing, or umbrella, potential, that is, to compute free energy

surfaces or to sample initial conditions at the transition state. In these cases, eq 1 is replaced with

$$H_n^{\text{umb}}(\mathbf{P}, \mathbf{Q}, \mathbf{p}_e, \mathbf{e}) = H_n(\mathbf{P}, \mathbf{Q}, \mathbf{p}_e, \mathbf{e}) + V_{\text{umb}}(\mathbf{Q}, \mathbf{e}) \quad (4)$$

where  $V_{\text{umb}}(\mathbf{Q}, \mathbf{e})$  is the umbrella potential, the precise form of which depends on the application (see section 3.2.1). Finally, we note that a Nosé–Poincaré thermostat<sup>32,33</sup> is applied for both the unbiased and biased vibrationally adiabatic dynamics.

### 2.1.2. Calculation of the Adiabatic Reaction Rate Constant.

In section 3, we present vibrationally adiabatic reaction rate constants determined using the reactive flux approach.<sup>24,25</sup> In these calculations, the dynamics are described by the classical Hamiltonian, eq 1, and the vibrational Schrödinger equation, eq 2. The vibrationally adiabatic reaction rate constant,  $k_f^{\text{ad}}$ , is then obtained from the evaluation of the reactive flux:

$$k_f^{\text{ad}} = \lim_{t \rightarrow \infty} \frac{\int d\mathbf{\Gamma} \dot{s} \delta(s) h(s(t)) e^{-\beta H_0}}{\int d\mathbf{\Gamma} h(-s) e^{-\beta H_0}} \quad (5)$$

where  $s$  is the reaction coordinate defined such that  $s = 0$  at the transition state and  $s > 0$  ( $s < 0$ ) corresponds to products (reactants),  $H_0$  is the ground state ( $n = 0$ ) vibrationally adiabatic Hamiltonian from eq 1,  $h(s)$  is the Heaviside step function, and  $\mathbf{\Gamma}$  represents the phase space variables. For the proton transfer reaction considered in this work, the reaction coordinate will be taken to be a collective solvent coordinate, that is,  $s = \Delta E = V_{gr}(r_A; \mathbf{Q}, \mathbf{e}) - V_{gr}(r_B; \mathbf{Q}, \mathbf{e})$  where  $r_A$  and  $r_B$  are taken to be representative proton positions for the reactants (“acid”) and products (“base”), respectively. Further, for this system,  $d\mathbf{\Gamma} = d\mathbf{P} d\mathbf{Q} d\mathbf{p}_e d\mathbf{e}$ .

The rate constant, eq 5, can be evaluated by dividing the calculation into two parts,<sup>24,25</sup> an equilibrium contribution representing the probability of reactants arriving at the transition state and a dynamical part that is the reactive flux associated with trajectories which have reached the transition state:

$$k_f^{\text{ad}} = \lim_{t \rightarrow \infty} \frac{\int d\mathbf{\Gamma} \dot{s} \delta(s) h(s(t)) e^{-\beta H_0}}{\int d\mathbf{\Gamma} \delta(s) e^{-\beta H_0}} \frac{\int d\mathbf{\Gamma} \delta(s) e^{-\beta H_0}}{\int d\mathbf{\Gamma} h(-s) e^{-\beta H_0}} \quad (6)$$

$$= \lim_{t \rightarrow \infty} \langle \dot{s} h(s(t)) \rangle_{\ddagger} P_{\text{re}}(s = 0) \quad (7)$$

Here,  $\langle \dots \rangle_{\ddagger}$  indicates an average over transition state configurations defined by  $s = \Delta E = 0$ . In practice, the probability of reactants reaching the transition state,  $P_{\text{re}}(s = 0)$ , is obtained from the adiabatic free energy calculations using the biased, umbrella sampling Hamiltonian of eq 4; see section 3.2.2.

**2.2. Vibrationally Nonadiabatic Dynamics. 2.2.1. Diabatic Representation.** In including the effect of nonadiabatic transitions on the reaction dynamics, we use a diabatic representation of the proton vibrational states. While in the application presented in section 3 we choose a two-state diabatic basis (intended to represent the two lowest proton vibrationally adiabatic states), an arbitrary number of states could be straightforwardly included. Within the diabatic basis, the proton vibrational wave function is thus written as

$$\Psi(r, \mathbf{Q}, \mathbf{e}) = \sum_{\alpha=1}^L c_{\alpha}(\mathbf{Q}, \mathbf{e}) \phi_{\alpha}(r) \quad (8)$$

where  $\phi_{\alpha}(r)$  are the diabatic states which are independent of the classical coordinates  $\mathbf{Q}$  and  $\mathbf{e}$ . The dynamics on diabatic state  $\alpha$  is then governed by the Hamiltonian

$$H_{\alpha}(\mathbf{P}, \mathbf{Q}, \mathbf{p}_e, \mathbf{e}) = \sum_i \frac{\mathbf{P}_i^2}{2m_i} + \sum_i \frac{\mathbf{p}_{e,i}^2}{2I_i} + \varepsilon_{\alpha}(\mathbf{Q}, \mathbf{e}) + \sum_i \lambda_i(\mathbf{e}_i \cdot \mathbf{e}_i - 1) \quad (9)$$

that differs from eq 1 only in the potential energy term,

$$\varepsilon_{\alpha}(\mathbf{Q}, \mathbf{e}) = \langle \phi_{\alpha} | \hat{h}_r(\hat{r}, \mathbf{Q}, \mathbf{e}) | \phi_{\alpha} \rangle_r \quad (10)$$

which is the proton vibrational energy for diabatic state  $\phi_{\alpha}$ .

If, as is done in section 3, two diabatic states are used, which we can denote as  $\alpha = \text{A}$  or  $\text{B}$  (e.g., “acid” corresponding to a vibrational state of  $\text{A}-\text{H} \cdots \text{B}$  character or “base” indicating a state describing  $\text{A}^{-} \cdots \text{H}-\text{B}$ ), these states, with energies given by eq 10, are coupled via diabatic coupling given by

$$\varepsilon_{\text{AB}}(\mathbf{Q}, \mathbf{e}) = \langle \phi_{\text{A}} | \hat{h}_r(\hat{r}, \mathbf{Q}, \mathbf{e}) | \phi_{\text{B}} \rangle_r \quad (11)$$

Note that the energies and this coupling are related to the vibrationally adiabatic Hamiltonian matrix by a unitary transformation:

$$\begin{pmatrix} E_0 & 0 \\ 0 & E_1 \end{pmatrix} = \mathbf{U}^T \begin{pmatrix} \varepsilon_{\text{A}} & \varepsilon_{\text{AB}} \\ \varepsilon_{\text{AB}} & \varepsilon_{\text{B}} \end{pmatrix} \mathbf{U} \quad (12)$$

where

$$\begin{pmatrix} \psi_0(r, \mathbf{Q}, \mathbf{e}) \\ \psi_1(r, \mathbf{Q}, \mathbf{e}) \end{pmatrix} = \mathbf{U} \begin{pmatrix} \phi_{\text{A}}(r) \\ \phi_{\text{B}}(r) \end{pmatrix} \quad (13)$$

Here, the adiabatic wave functions,  $\psi_n$ , and energies,  $E_n$ , are labeled by the vibrational state  $n$  as in eq 2. The unitary transformation is given by

$$\mathbf{U} = \begin{pmatrix} \cos \theta & \sin \theta \\ -\sin \theta & \cos \theta \end{pmatrix} \quad (14)$$

with

$$\theta = \frac{1}{2} \tan^{-1} \left[ \frac{2\varepsilon_{\text{AB}}}{\varepsilon_{\text{B}} - \varepsilon_{\text{A}}} \right] \quad (15)$$

and  $\theta = \theta(\mathbf{Q}, \mathbf{e})$  through the dependence of  $\varepsilon_{\text{A}}$ ,  $\varepsilon_{\text{B}}$ , and  $\varepsilon_{\text{AB}}$  on the classical coordinates  $\mathbf{Q}$  and  $\mathbf{e}$ .

**2.2.2. Classical Mapping Approach.** To describe the transitions between the proton vibrational states in this diabatic representation, we adopt the classical mapping approach.<sup>26–29</sup> This describes the nonadiabatic dynamics within a mean-field approximation, resulting in some shortcomings. However, it has two potential advantages from the point of view of reactive flux

calculations: (1) it gives time-reversible dynamics, and (2) its strength is in the description of strongly coupled regions, for example, the transition state of a proton transfer reaction where the fate of a trajectory is largely determined.

Classical mapping provides a convenient approach for describing the time evolution of the quantum wave function in a mixed quantum-classical framework. In particular, the proton wave function in the diabatic representation, eq 8, has its time-dependence expressed only in terms of the coefficients,  $c_{\alpha}(\mathbf{Q}, \mathbf{e}) = c_{\alpha}(t)$ , due to the time-dependence of the classical variables  $\mathbf{Q}(t)$  and  $\mathbf{e}(t)$ . The coefficients are determined by the time-dependent Schrödinger equation,

$$i\hbar \dot{c}_{\alpha}(t) = \sum_{\gamma} c_{\gamma}(t) \varepsilon_{\alpha\gamma} \quad (16)$$

where  $\varepsilon_{\alpha\gamma} = \langle \phi_{\alpha} | \hat{h}_r | \phi_{\gamma} \rangle_r$  are the diabatic state energies and couplings. In the classical mapping approach, one replaces the time-dependent complex coefficients,  $c_{\alpha}(t)$ , with real variables,  $X_{\alpha}$  and  $P_{\alpha}$ , such that

$$c_{\alpha}(t) = \frac{1}{\sqrt{2}} [X_{\alpha}(t) + iP_{\alpha}(t)] \quad (17)$$

Then,  $X_{\alpha}$  and  $P_{\alpha}$  behave as if they are the position and momenta variables of coupled harmonic oscillators.<sup>30</sup> The energy then becomes

$$E(\mathbf{Q}, \mathbf{e}, \{X_{\alpha}\}, \{P_{\alpha}\}) = \langle \Psi | \hat{h}_r | \Psi \rangle_r = \frac{1}{2} \sum_{\alpha,\gamma} [X_{\alpha} X_{\gamma} + P_{\alpha} P_{\gamma}] \varepsilon_{\alpha\gamma}(\mathbf{Q}, \mathbf{e}) \quad (18)$$

since  $\varepsilon_{\alpha\gamma} = \varepsilon_{\gamma\alpha}$ . The population,  $p_{\alpha}$ , of diabatic state  $\alpha$  is then related to the mapping variables  $X_{\alpha}$  and  $P_{\alpha}$  through

$$p_{\alpha} = c_{\alpha}^* c_{\alpha} = |c_{\alpha}|^2 = \frac{1}{2} (X_{\alpha}^2 + P_{\alpha}^2) \quad (19)$$

with the natural constraint  $\sum_{\alpha} p_{\alpha} = 1$ .

The nonadiabatic dynamics in this diabatic representation is governed by the classical mapping Hamiltonian

$$\tilde{H}(\mathbf{P}, \mathbf{Q}, \mathbf{p}_e, \mathbf{e}, \{X_{\alpha}\}, \{P_{\alpha}\}) = \sum_i \frac{\mathbf{P}_i^2}{2m_i} + \sum_i \frac{\mathbf{p}_{e,i}^2}{2I_i} + \frac{1}{2} \sum_{\alpha,\gamma} (X_{\alpha} X_{\gamma} + P_{\alpha} P_{\gamma}) \varepsilon_{\alpha\gamma}(\mathbf{Q}, \mathbf{e}) + \sum_i \lambda_i(\mathbf{e}_i \cdot \mathbf{e}_i - 1) \quad (20)$$

and the time-dependent Schrödinger equation is equivalent to solving a set of coupled Hamilton's equations in the classical mapping approach:

$$\frac{d\mathbf{Q}_i}{dt} = \nabla_{\mathbf{P}_i} \tilde{H} = \frac{\mathbf{P}_i}{m_i} \quad (21)$$

$$\frac{d\mathbf{e}_i}{dt} = \nabla_{\mathbf{p}_{e,i}} \tilde{H} = \frac{\mathbf{p}_{e,i}}{I_i} \quad (22)$$

$$\frac{d\mathbf{P}_i}{dt} = -\nabla_{\mathbf{Q}_i} \tilde{H} = -\frac{1}{2} \sum_{\alpha,\gamma} (X_\alpha X_\gamma + P_\alpha P_\gamma) \nabla_{\mathbf{Q}_i} \varepsilon_{\alpha\gamma}(\mathbf{Q}, \mathbf{e}) \quad (23)$$

$$\frac{d\mathbf{p}_{e,i}}{dt} = -\nabla_{\mathbf{e}_i} \tilde{H} = \mathbf{f}_{e,i} - 2\lambda_i \mathbf{e}_i \quad (24)$$

$$\mathbf{f}_{e,i}(t) \equiv -\frac{1}{2} \sum_{\alpha,\gamma} (X_\alpha X_\gamma + P_\alpha P_\gamma) \langle \phi_\alpha | \nabla_{\mathbf{e}_i} V_{\text{gr}}(r, \mathbf{Q}, \mathbf{e}) | \phi_\gamma \rangle_r$$

$$\frac{dX_\alpha}{dt} = \frac{\partial \tilde{H}}{\partial P_\alpha} = +P_\alpha \varepsilon_\alpha(\mathbf{Q}, \mathbf{e}) + \frac{1}{2} \sum_{\gamma \neq \alpha} P_\gamma [\varepsilon_{\alpha\gamma}(\mathbf{Q}, \mathbf{e}) + \varepsilon_{\gamma\alpha}(\mathbf{Q}, \mathbf{e})] \quad (25)$$

$$\frac{dP_\alpha}{dt} = -\frac{\partial \tilde{H}}{\partial X_\alpha} = -X_\alpha \varepsilon_\alpha(\mathbf{Q}, \mathbf{e}) - \frac{1}{2} \sum_{\gamma \neq \alpha} X_\gamma [\varepsilon_{\alpha\gamma}(\mathbf{Q}, \mathbf{e}) + \varepsilon_{\gamma\alpha}(\mathbf{Q}, \mathbf{e})] \quad (26)$$

The above equations can be implemented using, for example, a velocity Verlet algorithm.

If, as is the case for the proton transfer reaction considered in sections 3 and 4, only two states ( $\alpha = \text{A}$  or  $\text{B}$ ) are included in the description of the proton wave function, eqs 25 and 26 reduce to

$$\frac{dX_\alpha}{dt} = \frac{\partial \tilde{H}}{\partial P_\alpha} = +P_\alpha \varepsilon_\alpha(\mathbf{Q}, \mathbf{e}) + \frac{1}{2} P_\gamma [\varepsilon_{\alpha\gamma}(\mathbf{Q}, \mathbf{e}) + \varepsilon_{\gamma\alpha}(\mathbf{Q}, \mathbf{e})] \quad (27)$$

$$\frac{dP_\alpha}{dt} = -\frac{\partial \tilde{H}}{\partial X_\alpha} = -X_\alpha \varepsilon_\alpha(\mathbf{Q}, \mathbf{e}) - \frac{1}{2} X_\gamma [\varepsilon_{\alpha\gamma}(\mathbf{Q}, \mathbf{e}) + \varepsilon_{\gamma\alpha}(\mathbf{Q}, \mathbf{e})] \quad (28)$$

with a convention of  $\alpha \neq \gamma$ . It is then also sufficient to define a single variable,  $p$ , to represent the diabatic state populations. Here, our convention is that the acid, A (base, B) state is given by  $p = 0$  ( $p = 1$ ); that is,  $p$  is the base state population,  $p_B$ , in eq 19.

**2.2.3. Calculation of the Nonadiabatic Reaction Rate Constant.** Within this classical mapping description, the reaction rate constant can be calculated using the reactive flux approach as outlined in section 2.1.2 for vibrationally adiabatic dynamics, with two significant modifications. First, the vibrationally adiabatic Hamiltonian,  $H_0$ , is replaced by the classical mapping Hamiltonian,  $\tilde{H}$ , in eq 20. Second, the state populations, on which  $\tilde{H}$  depends, must be averaged over. This gives the nonadiabatic rate constant as

$$k_f^{\text{na}} = \lim_{t \rightarrow \infty} \frac{\int d\Gamma \int_0^1 dp \dot{s} \delta(s) h(s(t)) e^{-\beta \tilde{H}}}{\int d\Gamma \int_0^1 dp h(-s) e^{-\beta \tilde{H}}} \quad (29)$$

where, as before,  $s$  is the reaction coordinate (taken to be the collective solvent coordinate,  $\Delta E$ , defined in section 2.1.2) and  $\Gamma$

the phase space variables. As with the vibrationally adiabatic case, the rate constant can be divided into a dynamical part that is a measure of the time scale and probability of a trajectory starting at the transition state to form products and an equilibrium probability of reaching the transition state having started as a reactant:

$$k_f^{\text{na}} = \lim_{t \rightarrow \infty} \langle \dot{s} h(s(t)) \rangle' P'_{\text{re}}(s = 0) \quad (30)$$

However, here both quantities reflect the nonadiabaticity. Specifically, as indicated in eq 29, the dynamical contribution includes an averaging over the different state populations,  $p$ :

$$\langle \dot{s} h(s(t)) \rangle' = \frac{\int_0^1 dp \langle \dot{s} h(s(t)) \delta(p(0) - p) \rangle_{\ddagger} e^{-p\beta \Delta A_{\text{gap}}^{\ddagger}}}{\int_0^1 dp e^{-p\beta \Delta A_{\text{gap}}^{\ddagger}}} \quad (31)$$

Here,  $\Delta A_{\text{gap}}^{\ddagger} = \Delta A_1(s=0) - \Delta A_0(s=0)$  is the difference between the  $n=1$  and  $n=0$  vibrationally adiabatic Helmholtz free energies at the transition state; note that this is effectively the averaged vibrational energy gap at the transition state. The equilibrium part is obtained by assuming that the transition state vibrational states are in equilibrium and is thus given by

$$P'_{\text{re}}(s = 0) = \frac{\int ds \delta(s) e^{-\beta \Delta A_{\text{na}}(s)}}{\int ds h(-s) e^{-\beta \Delta A_{\text{na}}(s)}} \quad (32)$$

where

$$\Delta A_{\text{na}}(s) = -\frac{1}{\beta} \ln[e^{-\beta \Delta A_0(s)} + e^{-\beta \Delta A_1(s)}] \quad (33)$$

is the Helmholtz free energy associated with the thermally averaged nonadiabatic free energy surface. Note that the free energy surfaces are computed based on the vibrationally adiabatic states while the transition state sampling is obtained using vibrationally diabatic states; the mean field approximation of the classical mapping dynamics is used only for the dynamics of the trajectories initiated at the transition state.

### 3. Proton Transfer in a Nanoconfined Solvent

**3.1. System.** The proton transfer reaction complex considered in this work is a two valence-bond state description of a phenol–amine system, adapted from a model developed by Azzouz and Borgis.<sup>31</sup> Within the model, the phenol–amine hydrogen bond is constrained to be linear so that the proton motion occurs in one dimension,  $r$ , the phenol oxygen distance to the transferring proton. The electronic structure of the complex is taken to be in the electronically adiabatic limit; that is, only the ground electronic state is considered. To provide a description of the electronic ground state in the presence of the solvent molecules, a two valence bond state model is used. Specifically, the reaction complex is described by one valence bond state that is “neutral” in charge character, that is,  $\text{PhO}-\text{H} \cdots \text{NR}_3$ , and another that is of “ionic” character, that is,  $\text{PhO}^- \cdots \text{H}-\text{NR}_3^+$ . Their two energies,  $V_N(r, \mathbf{Q}, \mathbf{e})$  and  $V_I(r, \mathbf{Q}, \mathbf{e})$ , are modified by interaction with the nanoconfined solvent and, with the electronic coupling, determine the



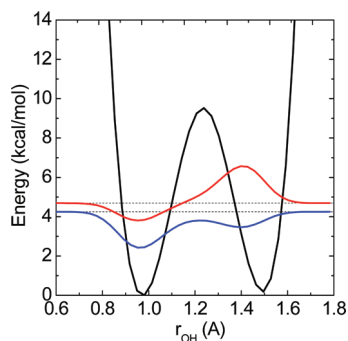


**Figure 1.** Vibrationally adiabatic proton wave functions at the transition state ( $\Delta E = 0$ ) along with their energy levels (dashed lines). The ground,  $\psi_0$  (blue), and first excited,  $\psi_1$  (red), adiabatic states are chosen as the diabatic vibrational states,  $\phi_A$  and  $\phi_B$ , respectively. Also shown is the proton potential (solid black line).

electronic ground state energy of the reaction complex for every solvent configuration.<sup>8</sup> From this electronic ground state, one can build up the vibrationally adiabatic, eq 1, diabatic, eq 9, and nonadiabatic, eq 20, Hamiltonians. The parameters for the proton transfer complex and the interactions between the complex and  $\text{CH}_3\text{Cl}$  solvent molecules are listed in Tables 1 and 2 of ref 8, with three exceptions: the heavy atom distance,  $d_{\text{ON}}$ , is set to 2.4 Å and the gas phase Morse parameters for the reaction complex,  $b_N$  and  $b_I$ , are 2.268 and 2.5 Å<sup>-1</sup>, respectively.

**3.2. Simulation Details.** The simulations are carried out with a single phenol–amine complex dissolved in nanoconfined  $\text{CH}_3\text{Cl}$  with a solution density of  $\sim 0.8 \text{ g/cm}^3$ , corresponding to 25  $\text{CH}_3\text{Cl}$  in the hydrophobic nanocavity of radius 10 Å. The molecular dynamics simulations were run with a time step of 1 fs for all simulations. The average temperature during the simulations is  $\sim 265 \text{ K}$  maintained by a Nosé–Poincaré thermostat<sup>33</sup> for the vibrationally adiabatic case and velocity rescaling<sup>34</sup> at every 8000 steps (8 ps) for the nonadiabatic case.

The vibrationally diabatic basis functions,  $\phi_A$  and  $\phi_B$ , are taken from the two lowest vibrationally adiabatic states of the proton determined from the proton potential at the transition state defined by  $\Delta E = 0$ , where  $\Delta E$  is the collective solvent coordinate defined in section 2.1.2. These wave functions are plotted in Figure 1. Specifically, the diabatic “acid,”  $\phi_A(r)$ , and “base,”  $\phi_B(r)$ , vibrational states are chosen to be the ground,  $\psi_0(r)$ , and first excited,  $\psi_1(r)$ , vibrationally adiabatic states, respectively. With this choice of diabatic basis states, the vibrationally diabatic energy matrix elements, can be explicitly calculated according to eqs 10 and 11.

**3.2.1. Free Energy Calculations.** Free energy curves along the collective solvent coordinate,  $\Delta E$ , were obtained using umbrella sampling with 13 bias potentials of the form  $V_{\text{umb}}^j = \frac{1}{2}k(\Delta E - \Delta E_j)^2$  with  $\Delta E_j = 0, \pm 1, \dots, \pm 4 \text{ kcal/mol}$  with  $k = 0.1 \text{ (kcal/mol)}^{-1}$  and  $\Delta E_j = \pm 8$  and  $\pm 16 \text{ kcal/mol}$  with  $k = 0.03 \text{ (kcal/mol)}^{-1}$ . A 1 ns trajectory was propagated for each  $\Delta E_j$  value with the transferring proton treated quantum mechanically in the vibrationally adiabatic ground state,  $n = 0$ , to yield  $\Delta A_0(\Delta E)$ . From this free energy surface, the vibrationally adiabatic excited state surface,  $\Delta A_1(\Delta E)$ , was obtained by adding the vibrational energy gap for each  $\Delta E$ . The classical free energy curve,  $\Delta A_{\text{cl}}(\Delta E)$ , was calculated by subtracting the vibrational zero point energy from  $\Delta A_0$ , and the vibrationally diabatic free energies were then determined by addition of  $\varepsilon_A(\Delta E)$  and  $\varepsilon_B(\Delta E)$  to the classical result. These free energy surfaces are shown in Figure 2. Errors were estimated based on 95% uncertainties using the Student  $t$  distribution with 10 blocks for each umbrella potential. The largest errors in the relevant region of the free

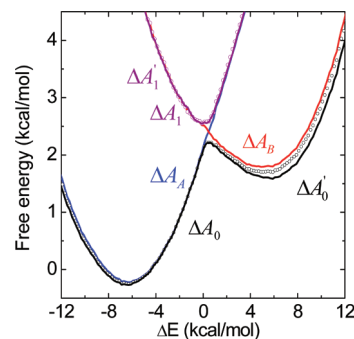


**Figure 2.** Vibrationally adiabatic,  $\Delta A_0$  (black line) and  $\Delta A_1$  (purple line), and diabatic,  $\Delta A_A$  (blue line) and  $\Delta A_B$  (red line), free energy curves versus  $\Delta E$ . The adiabatic state free energy curves obtained from the unitary transformation of the diabatic states in eq 12,  $\Delta A_0'$  (black circles) and  $\Delta A_1'$  (purple circles), are also shown for comparison.

energy curves,  $-12 \text{ kcal/mol} \leq \Delta E \leq 12 \text{ kcal/mol}$ , are less than 0.1 kcal/mol. To validate the use of the diabatic representation in the current approach, it is important that the directly computed adiabatic free energies and unitary-transformed free energies, eq 12, from the diabatic representation ( $\Delta A_0'$  and  $\Delta A_1'$ ) should be consistent. One can notice that this is indeed the case for the excited state ( $n = 1$ ) and for the ground state ( $n = 0$ ) in the reactant region, while there is a slight discrepancy in the product region of the ground state free energy surface.

**3.2.2. Reaction Rate Constant Calculations.** The reaction rate constants for the model phenol–amine proton transfer in nanoconfined  $\text{CH}_3\text{Cl}$  are obtained using eq 7 for the vibrationally adiabatic case and eq 30 for the nonadiabatic case. In both calculations, the dynamical contribution is obtained from trajectories initiated from the transition state defined by  $\Delta E = 0$ , where  $\Delta E$  is the collective solvent coordinate described in section 2.1.2. In the nonadiabatic case, trajectories are run with different initial vibrational state descriptions, that is, proton vibrational wave functions with different contributions of the diabatic states defined by  $p$ , as described in section 2.2.2. Five different initial diabatic vibrational states were considered:  $p = p_B = 0, 0.25, 0.50, 0.75$ , and 1. To obtain the initial conditions, an umbrella potential centered at  $\Delta E = 0$  was applied in the form discussed in section 3.2.1, but with a large force constant,  $k = 160 \text{ (kcal/mol)}^{-1}$ , and configurations with  $|\Delta E| < 0.001 \text{ kcal/mol}$  were collected. A total of 128 000 trajectories were used for the vibrationally adiabatic case, while 32 000 trajectories were used for each value of  $p$  for the nonadiabatic dynamics. Errors were calculated as 95% uncertainties using the Student  $t$  distribution based on the standard deviation obtained using 10 blocks of trajectories.

The total time of these trajectories initiated at the transition state should be sufficiently long so that no additional transition state recrossing is occurring. This is manifested as a plateau in the time-dependent rate constant given in eq 7 or 30. In practice, these times are relatively short, as can be seen from Figure 3. The plateau occurs at approximately 10 and 5 ps for the adiabatic and nonadiabatic cases, respectively. We note that no thermostat is used for these trajectories.

The other component of the rate constant is the probability of a reactant reaching the transition state,  $P_{\text{re}}(\Delta E = 0)$  in eq 7 for the adiabatic case and  $P'_{\text{re}}(\Delta E = 0)$  in eq 32 for the nonadiabatic case. These are obtained from the appropriate free energy surfaces, which are shown in Figure 4.

## 4. Results and Discussion

We have calculated the forward rate constant,  $k_f$ , for the model phenol–amine proton transfer reaction  $\text{Pho-H} \cdots \text{NR}_3 \rightleftharpoons$

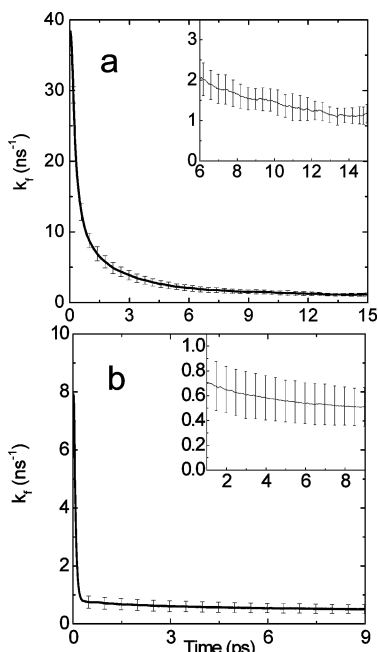


**Figure 3.** Time-dependent rate constants for the (a) adiabatic, eq 7, and (b) nonadiabatic, eq 30, cases. The long-time behavior is highlighted in the insets.

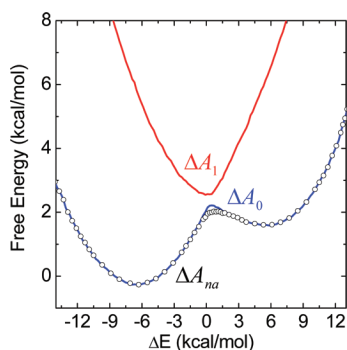


**Figure 4.** Probabilities at the transition state,  $P_{\text{re}}(\Delta E = 0)$  in eq 7 and  $P'_{\text{re}}(\Delta E = 0)$  in eq 33, obtained from the adiabatic ground free energy surface (in blue) and nonadiabatic free energy surface (black circles), respectively.

$\text{PhO}^- \cdots \text{H}-\text{NR}_3^+$  in a nanoconfined  $\text{CH}_3\text{Cl}$  solvent using the simulation approach described in section 3. While the rate constants are a key result, they are primarily interesting in that they allow us to determine the role of proton vibrational nonadiabaticity in the proton transfer reaction rate constant for this model system. In this context, we note that, in brief, the nonadiabatic rate constant,  $k_f^{\text{na}} = 0.50 \text{ ns}^{-1}$ , is less than half of the corresponding adiabatic rate constant,  $k_f^{\text{a}} = 1.2 \text{ ns}^{-1}$ , as can be seen from Figure 3 and Table 1.

We can understand this result in greater detail by examining the origins of the change in the rate constant. The rate constants and the other related quantities for both cases are listed in Table 1. We first focus on the relative contributions from the equilibrium and dynamical parts. It is interesting to note that the reactant probability density at the transition state,  $P_{\text{re}}(\Delta E = 0)$ , increases, from 0.0023 to 0.0031, when the vibrationally adiabatic excited ( $n = 1$ ) state is included in the nonadiabatic case. This results from the minimum in the  $n = 1$  state free energy,  $\Delta A_1(\Delta E)$ , around the transition state in contrast to the local maximum for the  $n = 0$  ground state. In other words, nonadiabaticity has the effect of slightly lowering the forward free energy barrier,  $\Delta A_f^\ddagger$ , from 2.5 to 2.3 kcal/mol. On the other

**TABLE 1: Comparison between the Proton Transfer Rate Constant,  $k_f$ , from Vibrationally Adiabatic and Nonadiabatic Calculations<sup>a</sup>**

	adiabatic	nonadiabatic
$k_f^{\text{a}}, k_f^{\text{na}} (\text{ns}^{-1})$	$1.2 \pm 0.2$	$0.50 \pm 0.16$
$P_{\text{re}}, P'_{\text{re}} (\text{kcal/mol})^{-1}$	0.0023	0.0031
$\langle \Delta \dot{E} h(\Delta E(t \rightarrow \infty)) \rangle_\ddagger (\text{kcal/mol/ps})$	$0.52 \pm 0.10$	$0.16 \pm 0.05$
$\Delta A_f^\ddagger (\text{kcal/mol})$	$2.48 \pm 0.08$	$2.29 \pm 0.08$
$\Delta A_b^\ddagger (\text{kcal/mol})$	$0.63 \pm 0.08$	$0.44 \pm 0.08$
$\kappa$	0.03	0.06

<sup>a</sup> The equilibrium,  $P_{\text{re}}(\Delta E = 0)$ ,  $P'_{\text{re}}(\Delta E = 0)$ , and dynamical,  $\langle \Delta \dot{E} h(\Delta E(t \rightarrow \infty)) \rangle_\ddagger$ , contributions to the rate constant, forward and backward free energy barriers,  $\Delta A_f^\ddagger$  and  $\Delta A_b^\ddagger$ , and transmission coefficient ( $\kappa = k_f/k_f^{\text{ST}}$ ) are also given.

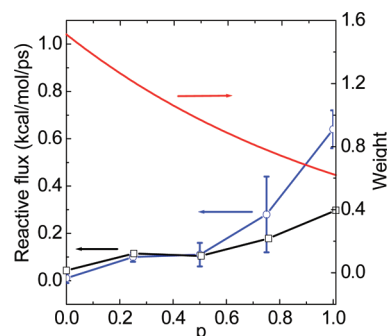


**Figure 5.** Reactive flux obtained with different initial diabatic vibrational states, defined by the population,  $p$  (blue line), along with the Boltzmann weighting of their contribution to the rate constant (red line) and the product of the two (black line) which is the direct contribution to the rate constant given by eq 31.

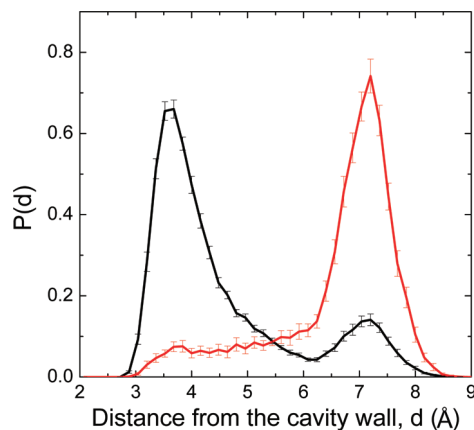
hand, the average reactive flux,  $\langle \Delta \dot{E} h(\Delta E(t \rightarrow \infty)) \rangle_\ddagger$ , decreases from 0.52 to 0.16 kcal/mol/ps when nonadiabaticity is included. This is because trajectories, especially those starting from the  $p = 0$  state, experience significant recrossings around the transition state due to nonadiabatic effects. Thus, while nonadiabaticity tends to enhance the rate constant by leading to more reactants reaching the transition state, it also suppresses the rate constant due to increased transition state recrossing. The latter dynamical factor plays a larger role than the former equilibrium factor in the present system, resulting in an overall decrease in the rate constant,  $k_f$ , from 1.2 to 0.50  $\text{ns}^{-1}$ . Since the reaction is endoergic ( $\Delta A_{\text{rxn}} = 1.9 \text{ kcal/mol}$ ) and the barrier for the backward reaction is rather low, the transmission coefficients are also low in both the adiabatic (0.03) and nonadiabatic (0.06) cases.

To further explore the issue of how nonadiabatic effects modify the rate constant, we examine the contribution to the nonadiabatic rate constant due to each diabatic state combination. In the context of the classical mapping approach, this can be done by comparing the results for different values of the “acid”/“base” diabatic state populations at the transition state as quantified by the parameter  $p$ . As shown in Figure 5, the contributions to the average flux from the proton state with  $p = 1$  or  $p = 0.75$  are greater than the contributions for  $p < 0.5$ ; this is still the case after the contributions are weighted by the appropriate Boltzmann factors. It is interesting to examine something akin to state-specific rate constants. Namely, since the diabatic coupling at the transition state is zero, the  $p = 0$  ( $p = 1$ ) state corresponds to the vibrationally adiabatic ground (or  $n = 1$ ) state there. Thus, the nonadiabatic rate constant initiated from  $p = 0$  or  $p = 1$  is that for transition states in the ground or excited vibrational state, respectively. These rate constants, assuming equal equilibrium contributions,

**TABLE 2: Contributions to the Nonadiabatic Rate Constant from Initial Vibrational States  $p = 0$  and 1, Which Are the Same As the Vibrationally Adiabatic States  $n = 0$  and  $n = 1$ , Respectively, at the Transition State<sup>a</sup>**

	$p = 0$	$p = 1$
$\langle \Delta \dot{E} h(\Delta E(t \rightarrow \infty)) \rangle_{\ddagger}$ (kcal/mol/ps)	$0.01 \pm 0.02$	$0.64 \pm 0.08$
$k_t$ (ns <sup>-1</sup> )	$0.03 \pm 0.06$	$2.01 \pm 0.25$
$\kappa$	0.0045	0.20

<sup>a</sup> For both cases,  $P'_{\text{re}}(\Delta E = 0)$  is taken to be the same as in Table 1.

**Figure 6.** Radial distributions of initial conditions as a function of the distance,  $d$ , from the nanocavity wall for trajectories that are in the product region at time  $t$  (see the text). Results are shown for  $t \rightarrow 0$  (black line) and  $t = 15$  ps (red line).

$P'_{\text{re}}(\Delta E = 0)$ , for the two cases, are given in Table 2. Interestingly, the nonadiabatic rate constant for  $p = 1$ , that is, the vibrationally excited transition state, is significantly greater than that for  $p = 0$ , for which  $k_t$  is not statistically different than zero. This indicates that flux through the vibrational ground state of the transition state ( $p = 0$ ) is more susceptible to nonadiabatic recrossing than flux through the vibrationally excited state, a point reinforced by the large difference in the transmission coefficients (see Table 2).

It was noted in section 1 that greater transition state recrossing can be observed for proton transfer reactions in nanoconfined solvents, and that is certainly the case for the system considered here. To investigate this point more quantitatively, we plot in Figure 6 the initial radial distribution of the proton transfer complex at the transition state ( $\Delta E = 0$ ) and compare it to the distribution obtained by selecting from those same initial conditions the ones which lead to products at a time  $t$  later ( $t = 15$  ps is shown). We note that the initial distribution is the same in form as the distribution of products for  $t \rightarrow 0$  (black curve in Figure 6) which is simply that for trajectories initiated at the transition state with positive momentum at  $t = 0$ . The product distribution in this short time limit thus reflects both the available volume and the free energy as a function of the reaction complex radial position at the transition state defined by  $\Delta E = 0$ . The former favors positions near the cavity wall where there is more available volume ( $V_{\text{avail}} = 4\pi(R - d)^2$ , where  $R$  is the cavity radius and  $d$  the distance from the cavity wall). The combination of the free energy and available volume leads to more trajectories initiated near the cavity wall rather than in the interior of the cavity. The difference between the distribution at  $t \rightarrow 0$  and at a time  $t$  later reflects the dependence of transition state recrossing on the reaction complex radial position in the cavity. For example, the distribution at a time  $t$  would be the same as that at time  $t \rightarrow 0$  if recrossing was uniform throughout

the cavity. However, it is clear from the  $t = 15$  ps distribution in Figure 6 that in reality many of trajectories that pass through the transition state near the cavity wall eventually recross and return to the reactant region, a natural consequence of the less favorable reaction free energy reaction near the wall compared to the interior.<sup>35</sup> On the other hand, the trajectories which pass through the transition state nearer the center of the cavity recross significantly less, leading to the peak in the  $t = 15$  ps distribution nearer the cavity center.

Finally, it is useful to consider the present results in the context of previous studies. The Azzouz–Borgis model,<sup>31</sup> on which our two valence bond state model is based, has been used by many researchers as a test problem for calculating proton transfer reaction rate constants in bulk liquids by a variety of methods. These include mixed quantum-classical surface hopping,<sup>11</sup> variational transition state theory with multidimensional tunneling corrections,<sup>36</sup> various flavors of quantum mechanical analogs of transition state theory,<sup>37</sup> a mixed quantum-classical Liouville approach,<sup>16</sup> and ring polymer molecular dynamics.<sup>38</sup> Although the specific methods differ, all are intended to include quantum mechanical effects and all yield reaction rate constants larger than the corresponding classical value. It is interesting to note that there is still some significant disagreement between the results from different methods<sup>37,38</sup> with proton transfer rate constants varying by up to a factor of 2 and deuteron transfer rate constants by as much as a factor of 8, giving estimated kinetic isotope effects from  $\sim 4$  to  $\sim 50$ .

In this paper, we report particularly on the effect of vibrational nonadiabaticity on the rate constant, an effect first explored by Hammes-Schiffer and Tully.<sup>11</sup> They included nonadiabatic transitions with a surface hopping approach and found the nonadiabatic rate constant ( $77 \text{ ns}^{-1}$ ) to be smaller than the corresponding adiabatic rate constant ( $180 \text{ ns}^{-1}$ ) by a factor of  $\sim 2.3$ . They attributed this to increased transition state recrossing; that is, nonadiabatic transitions in the transition state region lead to dynamics in a vibrationally excited state that does not promote reaction but rather returns trajectories to the reactant region. More recently, Hanna and Kapral<sup>16</sup> have used a mixed quantum-classical Liouville approach to calculate rate constants for the same system. While they obtained different quantitative results, they found that including nonadiabatic results also led to a smaller rate constant ( $35 \text{ ns}^{-1}$ ) than a purely vibrationally adiabatic treatment ( $47 \text{ ns}^{-1}$ ). These results are in qualitative agreement with the present results for a similar, but modified model for the proton transfer complex in a confined solvent, in which the nonadiabatic rate constant ( $0.50 \text{ ns}^{-1}$ ) is also found to be smaller than the adiabatic one ( $1.2 \text{ ns}^{-1}$ ). This indicates that there is not a dramatic change in the effect of vibrationally nonadiabatic transitions on the rate constant in a nanoconfined solvent compared to in the bulk solvent. Moreover, the origin, increased transition state recrossing, is also the same, which we have determined from our calculation of the reactive flux (see Table 1). However, as noted above, we have observed another effect that modifies the nonadiabatic rate constant but was not present in these other studies: an equilibrium contribution that includes a nonzero probability of finding the system in the vibrationally excited state at the transition state. This effect acts to increase the nonadiabatic rate constant, but is smaller in magnitude than that associated with the increased transition state recrossing. Indeed, we have estimated that if we only started trajectories at the transition state in the vibrational ground state, the nonadiabatic rate constant would be significantly smaller.



## 5. Concluding Remarks

We have employed a classical mapping approach within reactive flux calculations to investigate nonadiabatic effects in the reaction rate constant of a model proton transfer complex in a nanoconfined solvent. The key results are summarized below.

Inclusion of nonadiabatic effects results in a reduction in the proton transfer rate constant by a factor of 2.4 for the model phenol–amine system considered here in a nanoconfined methyl chloride solvent. This result is consistent with the usual suggestion that including nonadiabatic transitions will lead to more transition state recrossing, as discussed in section 4.

The effect and relative magnitude of equilibrium and dynamical contributions have been examined in detail. It is found that they compete in their influence on the rate constant. Specifically, including nonadiabaticity in the calculation of the equilibrium contribution enhances the rate constant, that is, assuming vibrationally nonadiabatic behavior makes the transition state more accessible thermodynamically. This nonadiabatic effect in the equilibrium part has often been ignored in other works where it is assumed all trajectories at the transition state start in the vibrational ground state. On the other hand, including nonadiabatic transitions in the dynamics of the trajectories initiated at the transition state decreases the reactive flux due to increased transition state recrossing. That is, allowing changes in the proton vibrational state tends to increase the likelihood of recrossing, since, for example, the vibrationally adiabatic excited state does not lead to reaction unlike the ground state (see Figure 4). The reduction of the rate constant due to this dynamical contribution is greater than the enhancement due to the thermodynamical contribution, resulting in the smaller nonadiabatic rate constant compared to the adiabatic result.

Finally, the consequences of ignoring initial conditions involving vibrationally excited states were also investigated. For this purpose, the hypothetical nonadiabatic rate constant which precludes any possible contribution from the excited vibrational state at the transition state was computed and compared to the full nonadiabatic rate constant. These two results are dramatically different. Thus, for this system, which has a relatively small vibrational splitting at the transition state, including the contribution from an excited vibrational state at the transition state is necessary to calculate an accurate nonadiabatic rate constant. The magnitude of this contribution in other systems will naturally depend on the vibrational energy gap at the transition state and the nonadiabatic coupling, but the present results indicate that it should not be ignored a priori.

**Acknowledgment.** This work was supported by the Chemical Sciences, Geosciences, and Biosciences Division, Office of Basic Energy Sciences, Office of Science, U.S. Department of Energy.

## References and Notes

- (1) (a) Das, S.; Datta, A.; Bhattacharyya, K. *J. Phys. Chem. A* **1997**, *101*, 3299–3304. (b) Mandal, D.; Pal, S. K.; Bhattacharyya, K. *J. Phys. Chem. A* **1998**, *102*, 9710–9714. (c) Pal, S. K.; Mandal, D.; Bhattacharyya, K. *J. Phys. Chem. B* **1998**, *102*, 11017–11023.

- (2) Cohen, B.; Huppert, D.; Solntsev, K. M.; Tsfadia, Y.; Nachliel, E.; Gutman, M. *J. Am. Chem. Soc.* **2002**, *124*, 7539–7547.
- (3) (a) Bardez, E.; Goguillon, B.-T.; Keh, E.; Valeur, B. *J. Phys. Chem.* **1984**, *88*, 1909–1913. (b) Bardez, E.; Monnier, E.; Valeur, B. *J. Phys. Chem.* **1985**, *89*, 5031–5036.
- (4) (a) Politi, M. J.; Brandt, O.; Fendler, J. H. *J. Phys. Chem.* **1985**, *89*, 2345–2354. (b) Politi, M. J.; Chaimovich, H. *J. Phys. Chem.* **1986**, *90*, 282–287.
- (5) Kwon, O.-H.; Jang, D.-J. *J. Phys. Chem. B* **2005**, *109*, 8049–8052.
- (6) Prossposito, P.; Marks, D.; Zhang, H.; Glasbeek, M. *J. Phys. Chem. A* **1998**, *102*, 8894–8902.
- (7) McKiernan, J.; Simoni, E.; Dunn, B.; Zink, J. I. *J. Phys. Chem.* **1994**, *98*, 1006–1009.
- (8) Li, S.; Thompson, W. H. *J. Phys. Chem. B* **2005**, *109*, 4941–4946.
- (9) Thompson, W. H. *J. Phys. Chem. B* **2005**, *109*, 18201–18208.
- (10) Rodriguez, J.; Martí, J.; Guàrdia, E.; Laria, D. *J. Phys. Chem. B* **2007**, *111*, 4431–4439.
- (11) Hammes-Schiffer, S.; Tully, J. C. *J. Chem. Phys.* **1994**, *99*, 4657–4667.
- (12) Hammes-Schiffer, S.; Tully, J. C. *J. Phys. Chem.* **1995**, *99*, 5793–5797.
- (13) Hammes-Schiffer, S. *J. Phys. Chem. A* **1998**, *102*, 10443–10454.
- (14) Fang, J.-Y.; Hammes-Schiffer, S. *J. Chem. Phys.* **1999**, *110*, 11166–11175.
- (15) Coker, D. F. In *Computer Simulation in Chemical Physics*; Allen, M. P.; Tildesley, D. J., Eds.; NATO ASI, Kluwer: Dordrecht, 1993; pp 315–377.
- (16) Hanna, G.; Kapral, R. *J. Chem. Phys.* **2005**, *122*, 244505.
- (17) Nakamura, H. In *Dynamics of Molecules and Chemical Reactions*; Wyatt, R. E.; Zhang, J. Z. H., Eds.; Marcel Dekker, Inc.: New York, 1996; pp 473–529.
- (18) (a) Prezhdo, O. V.; Rossky, P. J. *J. Chem. Phys.* **1997**, *107*, 825–834. (b) Wong, K. F.; Rossky, P. J. *J. Phys. Chem. A* **2001**, *105*, 2546–2556.
- (19) (a) Bittner, E. R.; Rossky, P. J. *J. Chem. Phys.* **1995**, *103*, 8130–8143. (b) Schwartz, B. J.; Bittner, E. R.; Prezhdo, O. V.; Rossky, P. J. *J. Chem. Phys.* **1996**, *104*, 5942–5955. (c) Bittner, E. R.; Rossky, P. J. *J. Chem. Phys.* **1997**, *107*, 8611–8618. (d) Prezhdo, O. V.; Rossky, P. J. *J. Chem. Phys.* **1997**, *107*, 5863–5878.
- (20) Sun, X.; Wang, H.; Miller, W. H. *J. Chem. Phys.* **1998**, *109*, 7064–7074.
- (21) Ka, J.; Shin, S. *J. Chem. Phys.* **1998**, *109*, 10087–10095.
- (22) Tully, J. C. *J. Chem. Phys.* **1990**, *93*, 1061–1071.
- (23) Hammes-Schiffer, S.; Tully, J. C. *J. Chem. Phys.* **1995**, *103*, 8528–8537.
- (24) Chandler, D. *J. Chem. Phys.* **1978**, *68*, 2959–2970.
- (25) Frenkel, D.; Smit, B. *Understanding Molecular Simulation*; Academic: San Diego, 1996.
- (26) (a) Miller, W. H.; McCurdy, C. W. *J. Chem. Phys.* **1978**, *69*, 5163–5173. (b) McCurdy, C. W.; Meyer, H.-D.; Miller, W. H. *J. Chem. Phys.* **1979**, *70*, 3177–3187.
- (27) (a) Meyer, H.-D.; Miller, W. H. *J. Chem. Phys.* **1979**, *71*, 2156–2169. (b) Meyer, H.-D.; Miller, W. H. *J. Chem. Phys.* **1980**, *72*, 2272–2281.
- (28) Meyer, H.-D.; Miller, W. H. *J. Chem. Phys.* **1979**, *70*, 3214–3223.
- (29) (a) Stock, G.; Thoss, M. *Phys. Rev. Lett.* **1997**, *78*, 578–581. (b) Thoss, M.; Stock, G. *Phys. Rev. A* **1999**, *59*, 64–79.
- (30) Strocchi, F. *Rev. Mod. Phys.* **1966**, *38*, 36–40.
- (31) Azzouz, H.; Borgis, D. *J. Chem. Phys.* **1993**, *98*, 7361–7375.
- (32) Thompson, W. H. *J. Chem. Phys.* **2003**, *118*, 1059–1067.
- (33) Bond, S. D.; Leimkuhler, B. J.; Laird, B. B. *J. Comput. Phys.* **1999**, *151*, 114–134.
- (34) Allen, M. P.; Tildesley, D. J. *Computer Simulation of Liquids*; Oxford University Press: New York, 1987.
- (35) Thompson, W. H. *J. Chem. Phys.* **2002**, *117*, 6618–6628.
- (36) McRae, R. P.; Schenter, G. K.; Garrett, B. C.; Svetlicic, Z.; Truhlar, D. G. *J. Chem. Phys.* **2001**, *115*, 8460–8480.
- (37) Yamamoto, T.; Miller, W. H. *J. Chem. Phys.* **2005**, *122*, 044106.
- (38) Collepardo-Guevara, R.; Craig, I. R.; Manolopoulos, D. E. *J. Chem. Phys.* **2008**, *128*, 144502.

JP911740C